Tetrazine-Functionalized UiO-68 for Highly Selective Au(III) Recovery from Acidic Solutions

Zhuoran Sun[a], Yali Ma*[a], Haijun Hu[b], Xue Zhou[b], Peng Jiang[a], Xue Li[a], Jiyang Li[c], Yunling Liu[c] and Xiaodong Sun*[b]

a College of Chemical Engineering, Shenyang University of Chemical Technology, Shenyang 110142, P. R. China

b Institute of Clean Energy Chemistry, Key Laboratory for Green Synthesis and Preparative Chemistry of Adv. Mater., College of Chemistry, Liaoning University, Shenyang 110036, People's Republic of China

c State Key Laboratory of Inorganic Synthesis and Preparative Chemistry, College of Chemistry, Jilin University, Changchun 130012, P.R. China

**Corresponding author.*

E-mail address: maylchem@syuct.edu.cn; sunxiaodong@lnu.edu.cn

1. Characterization

Powder X-ray diffraction (PXRD) patterns were recorded on a Rigaku SmartLab SE diffractometer (Rigaku, Japan) using a Cu target in the 2θ range of 3–40° at a scan rate of 2° min^{-1}, with a tube voltage of 40 kV and a current of 40 mA. The thermal stability of the MOFs was characterized by simultaneous thermal analysis on a HITACHI STA200 instrument (Hitachi, Japan) in air from 30 to 800 °C at a heating rate of 10 °C·min^{-1}. X-ray photoelectron spectroscopy (XPS) measurements were carried out on a Shimadzu/Kratos AXIS Ultra DLD spectrometer, and high-resolution spectra of each element were collected by measuring its most intense core-level peak. Fourier transform infrared (FT-IR) spectra were recorded on a Nicolet iS20 FT-IR spectrometer (Thermo Fisher Scientific, USA) in the range of 4000–400 cm^{-1} with a resolution of 4 cm^{-1}, using the KBr pellet technique. The morphology of the samples was examined by scanning electron microscopy (SEM) on a GeminiSEM 300 microscope (ZEISS, Germany). Prior to SEM observation, the samples were dispersed in ethanol and ultrasonicated for 10 min to obtain a uniform dispersion on the substrate. The concentrations of metal ions in solution were determined by inductively coupled plasma optical emission spectrometry (ICP-OES, Agilent 5110, Agilent Technologies, USA) after appropriate dilution, and the resulting data were used to evaluate the adsorption performance of the materials toward metal ions.

2. Effect of pH on Au(III) adsorption

The effect of solution pH on the adsorption performance was investigated using an Au(III) solution with an initial concentration of 100 mg/L. The pH was adjusted to the

desired value with dilute NaOH solution, followed by ultrasonication to ensure thorough mixing. In each run, 4.0 mg of adsorbent was added into 4.0 mL of the Au(III) solution, corresponding to a dosage of 1.0 g/L. The suspensions were stirred magnetically at the preset pH for 2 h, and then centrifuged to separate the solid and liquid phases. The residual Au(III) concentration in the supernatant was determined by ICP-OES, and the equilibrium adsorption capacity was calculated accordingly.

3. Adsorption kinetic models

To gain deeper insight into the adsorption rate of Au(III) on the two adsorbents and to identify the rate-controlling steps, the experimental kinetic data were fitted using three commonly applied models: the pseudo-first-order model, the pseudo-second-order model, and the intraparticle diffusion model.[1] The corresponding equations and parameter definitions are summarized below.

3.1. Pseudo-first-order kinetic model

The pseudo-first-order model assumes that the adsorption rate is proportional to the number of vacant adsorption sites. Its linear form can be expressed as:

$$\ln\left(q_e - q_t\right) = \ln\left(q_e\right) - k_1 t \#(S1)$$

where q_e and q_t (mg/g) are the adsorption capacities at equilibrium and at time t, respectively; t (min) is the contact time; and k_1 (min^{-1}) is the pseudo-first-order rate constant. A plot of ln (q_e-q_t) versus t allows the evaluation of k_1 and the theoretical q_e from the slope and intercept.

3.2. Pseudo-second-order kinetic model

The pseudo-second-order model is often employed to describe systems where the

overall rate is closely related to surface processes such as chemisorption or coordination. Its linear equation is given by:

$$\frac{t}{q_t} = \frac{1}{k_2 q_e^2} + \frac{t}{q_e} \#(S2)$$

where k_2 (g/mg/min) is the pseudo-second-order rate constant, and q_e and q_t have the same meanings as above. By plotting t/q_t against t, the slope and intercept can be used to obtain the theoretical equilibrium uptake q_e and the rate constant k_2. When the experimental data are better described by this model, it generally indicates that chemical interactions play a dominant role in the rate-controlling step.

3.3. Intraparticle diffusion model

To evaluate the contribution of diffusion within the pores or particles to the overall adsorption process, the intraparticle diffusion model was further applied. It can be written as:

$$q_t = k_3 t^{(1/2)} + C \#(S3)$$

where k_3 (mg/g/min$^{1/2}$) is the intraparticle diffusion rate constant, and C is a constant associated with the thickness of the boundary layer. When a plot of q_t versus $t^{1/2}$ yields a straight line that passes (or nearly passes) through the origin ($C \approx 0$), intraparticle diffusion can be regarded as the main rate-controlling step.

3.4. Arrhenius equation

The activation energy (E_a) can be used to indicate whether the interaction between the adsorbent and the metal ions during adsorption is predominantly physical or involves chemical reaction. The Arrhenius equation was as follows:[2]

$$\ln k_2 = -\frac{E_a}{RT} + \ln A \#(S4)$$

where A is the Arrhenius constant (g/mg·min), E_a denotes the activation energy for sorption (kJ/mol), R is the universal gas constant (8.314 J/mol·K), and T represents the absolute temperature (K).

4. Adsorption thermodynamics

The thermodynamic parameters for Au(III) adsorption were evaluated using the Gibbs free energy equation and the van′t Hoff relationship.[2,3] The Gibbs free energy expression is given as:

$$\Delta G = -RT\ln\left(1000K_c\right)\#(S5)$$

The van't Hoff equation is given as:

$$\ln\left(1000K_c\right) = -\frac{\Delta H}{RT} + \frac{\Delta S}{R}\#(S6)$$

where T denotes the absolute temperature (K) and R is the universal gas constant (8.314 J/mol K). The equilibrium constant was taken as $K_c = q_e/C_e$. According to the van't Hoff relationship, △H and △S were extracted from the linear regression of $ln(1000kc)$ against $1/T$.

5. Ion-selectivity experiments

The adsorption selectivity of UiO-68-TZDC toward Au(III) was evaluated in the presence of coexisting Fe^{3+}, Cu^{2+}, and K^+ ions. A mixed solution containing Au(III), Fe^{3+}, Cu^{2+}, and K^+ was prepared, and the initial concentration of each ion was adjusted to 200 mg/L. In each run, 4.0 mg of adsorbent was added into 4.0 mL of the mixed-ion solution, corresponding to a dosage of 1.0 g/L. The suspensions were magnetically stirred for 2 h under the preset conditions, and then centrifuged to separate the solid and liquid phases. The residual concentrations of Au(III), Fe, Cu, and K in the supernatant

were determined by ICP-OES, and the removal efficiency and selectivity parameters for Au(III) were calculated accordingly.

Based on the residual concentrations determined by ICP-OES, the distribution coefficient (D, i.e., K_d) for each metal ion and the selectivity coefficient $K_{Au/M}$ for Au(III) were calculated to quantitatively describe their partitioning between the solid and liquid phases. The corresponding equations are given below.[4]

$$D = \frac{C_0 - C_e}{C_e} \times \frac{V}{W} \#(S7)$$

$$k = \frac{D_{Au}}{D_M} \#(S8)$$

Where C_0 and C_e (mg/L) are the initial and equilibrium concentrations of the target ion in solution, respectively; V (L) is the solution volume; W (g) is the mass of adsorbent; D_{Au} and D_M (L/g) are the distribution coefficients of Au(III) and the competing metal ion M (e.g., Fe(III), Cu(II)), respectively; and $k_{Au/M}$ is the selectivity coefficient of Au(III) over the competing ion M (dimensionless).

6. Reusability (adsorption–desorption) experiments

The reusability and regeneration ability of UiO-68-TZDC were evaluated through repeated adsorption–desorption cycles. In each cycle, 30 mg of adsorbent was added to 50 mL of Au(III) solution with an initial concentration of 100 mg/L, and the suspension was magnetically stirred for 24 h to achieve adsorption equilibrium. The solid was then recovered by centrifugation and subjected to desorption using a freshly prepared thiourea–hydrochloric acid solution. The desorption solution was prepared by dissolving 5 g thiourea and 5.68 mL concentrated HCl (37%) in 30 mL deionized water and diluting the mixture to 50 mL.

The separated adsorbent was dispersed in this desorption solution and magnetically stirred for 3 h. After desorption, the solid was washed with deionized water three times and methanol twice, followed by drying at room temperature. The regenerated material was then used for the next adsorption cycle. The Au(III) concentration after each cycle was determined by ICP-OES to calculate the retention of adsorption capacity.

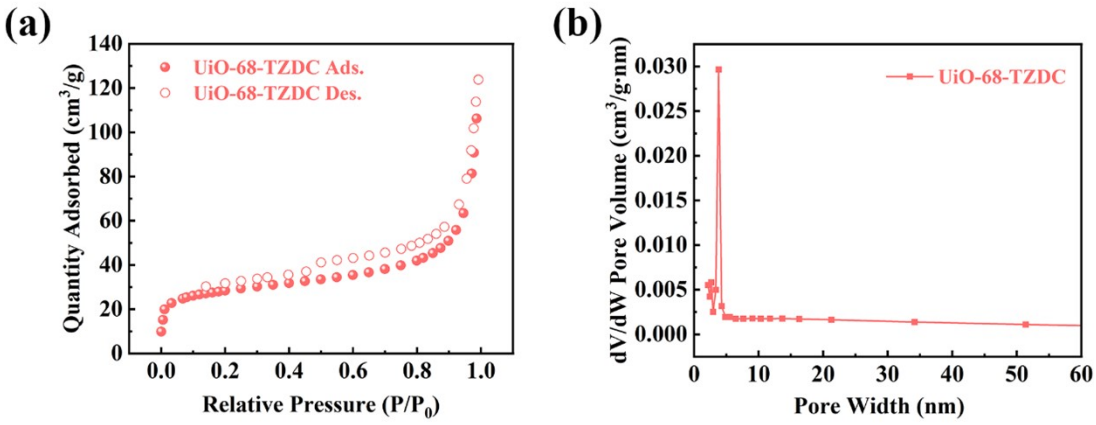

Fig. S1. (a) N_2 adsorption–desorption isotherms of UiO-68-TZDC measured at 77 K. (b) Pore size distribution of UiO-68-TZDC derived from the N_2 adsorption data.

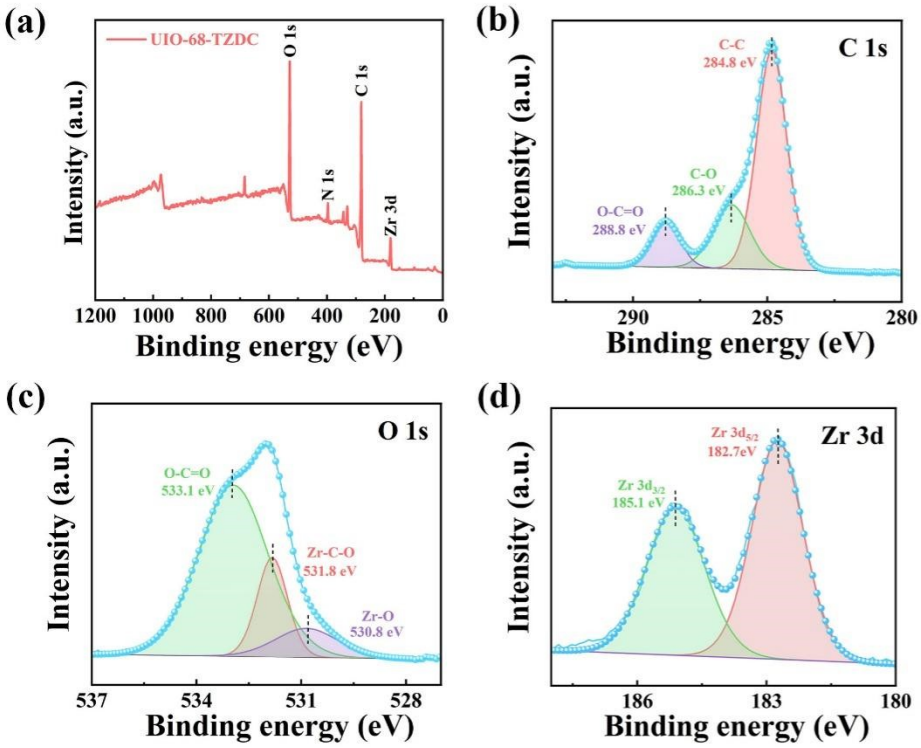

Fig. S2. XPS spectra of UiO-68-TZDC.

(a) Survey spectrum of UiO-68-TZDC showing the main Zr, O, C and N signals characteristic of UiO-68-type Zr_6 clusters coordinated by organic linkers. (b) High-resolution C 1s spectrum deconvoluted into three components at 284.8 eV (C–C), 286.3 eV (C–O) and 288.8 eV (O–C=O), consistent with aromatic carbons and carboxylate groups of the TZDC linker. (c) High-resolution O 1s spectrum fitted with peaks at 533.1 eV (O–C=O in carboxylates), 531.8 eV (Zr–C–O) and 530.8 eV (Zr–O). (d) High-resolution Zr 3d spectrum showing a Zr $3d_{5/2}$–Zr $3d_{3/2}$ doublet at 182.7 and 185.1 eV, confirming the successful formation of the UiO-68-TZDC framework.

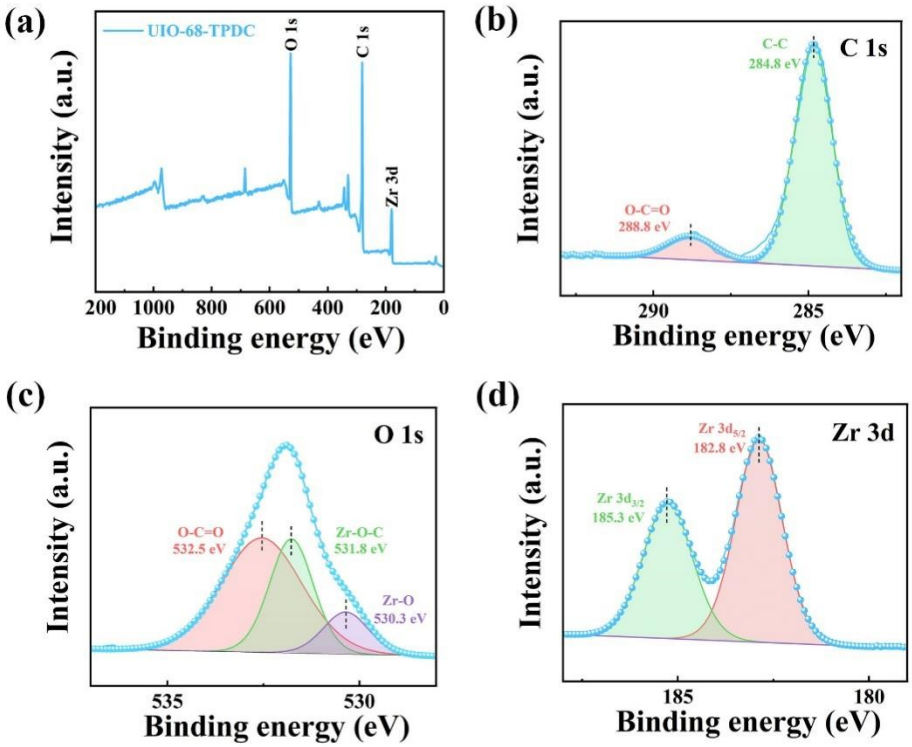

Fig. S3. XPS spectra of UiO-68-TPDC.

(a) Survey spectrum of UiO-68-TPDC showing the main C, O and Zr signals arising from the organic linker and Zr_6 nodes. (b) High-resolution C 1s spectrum, which can be deconvoluted into two main components at 284.8 eV and 288.8 eV, assigned to aromatic C–C species and carboxylate O–C=O groups of the TPDC linker, respectively. (c) High-resolution O 1s spectrum fitted with three contributions at 530.3 eV (coordinated O in Zr–O clusters), 531.8 eV (Zr–O–C) and 532.5 eV (O–C=O in coordinated carboxylates), reflecting the mixed oxide-carboxylate environment around the Zr_6 clusters. (d) High-resolution Zr 3d spectrum displaying a Zr $3d_{5/2}$–Zr $3d_{3/2}$ doublet at approximately 182.8 and 185.3 eV, confirming the successful synthesis of UiO-68-TPDC.

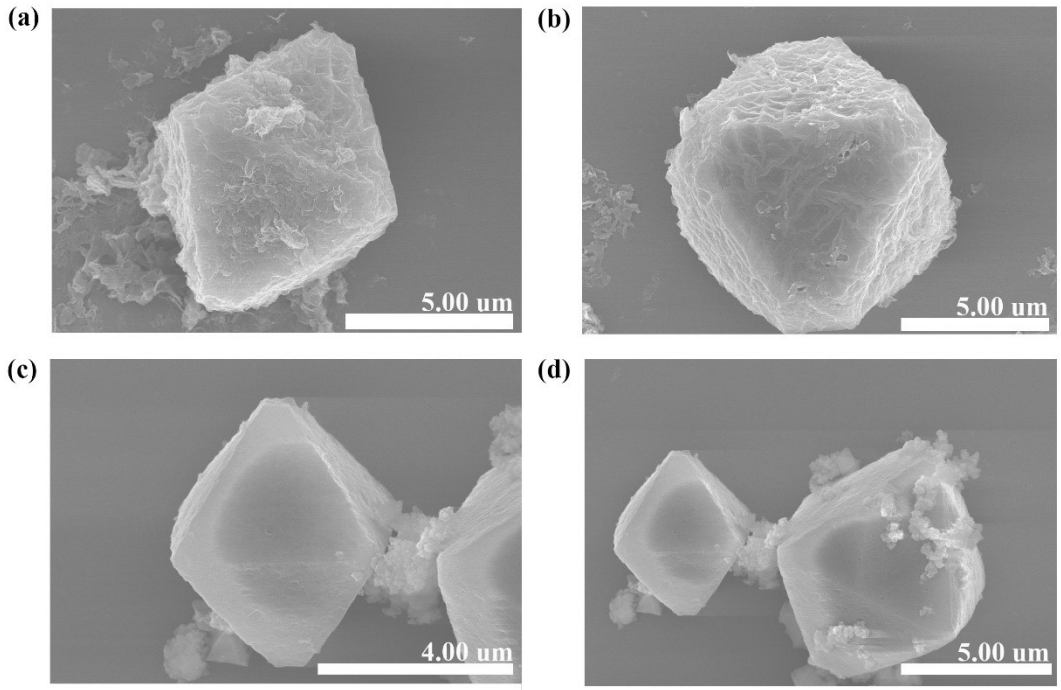

Fig. S4. SEM images of (a-b) UiO-68-TZDC and (c-d) UiO-68-TPDC.

As shown in Fig. S4, both adsorbents exhibit a well-defined octahedral crystal morphology, which is consistent with the typical crystal features of the UiO-68 framework.

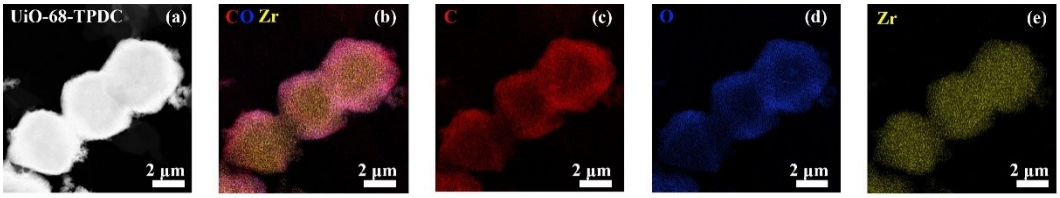

Fig. S5. TEM-EDS characterization of UiO-68-TPDC: (a) TEM image; (b) overlapped C/O/Zr elemental mapping; (c-e) individual maps of C, O and Zr.

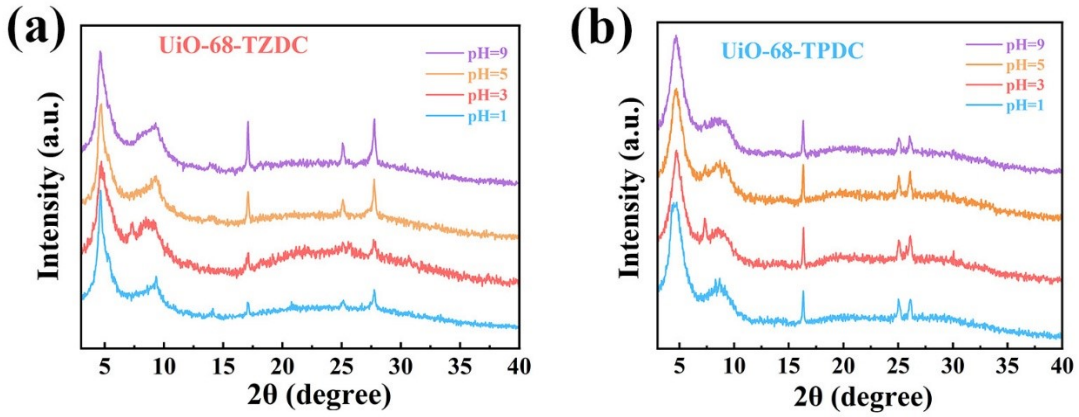

Fig. S6. PXRD patterns of UiO-68-TZDC (a) and UiO-68-TPDC (b) after magnetic stirring for 2 h in aqueous solutions with different pH values (pH = 1–9). The activated samples were dispersed in water, and the pH was adjusted to the desired value using dilute HCl or NaOH, followed by magnetic stirring at room temperature for 2 h. After the treatment, the solids were collected by centrifugation, washed thoroughly with deionized water, and vacuum-dried for 24 h before PXRD measurements. The diffraction peaks are largely preserved over the entire pH range, with only minor intensity variations at extreme pH, indicating that both Zr-MOFs retain their crystallinity and framework integrity under acidic to mildly basic aqueous conditions.

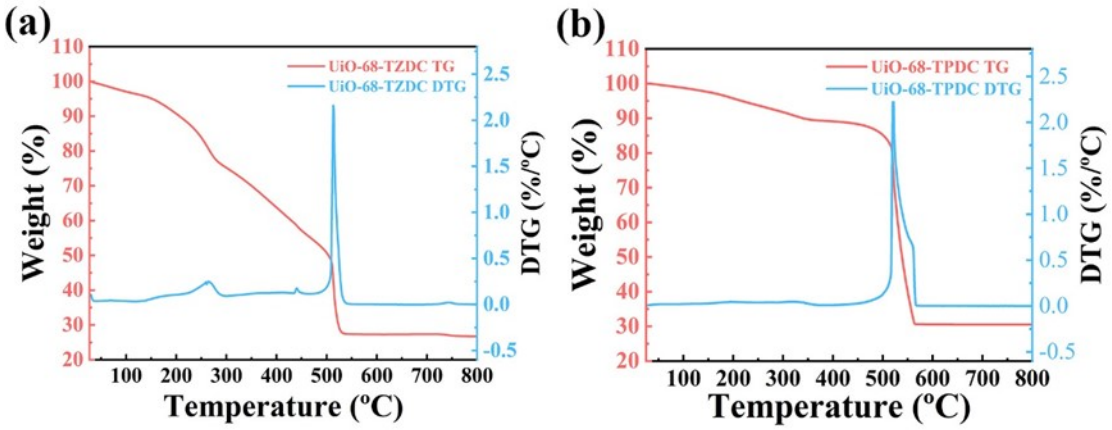

Fig. S7. (a) TG/DTG curves of UiO-68-TZDC and (b) UiO-68-TPDC.

The measurements were carried out in air from 30 to 800 °C at a heating rate of 10 °C·min^{-1}. The slight mass loss below about 150 °C is mainly attributed to the removal of solvent molecules and crystallization water in the materials, while the pronounced weight loss and strong DTG peak around 500–600 °C correspond to the decomposition of the organic linkers and the collapse of the Zr_6 framework, indicating that both adsorbents exhibit good thermal stability up to about 500 °C.

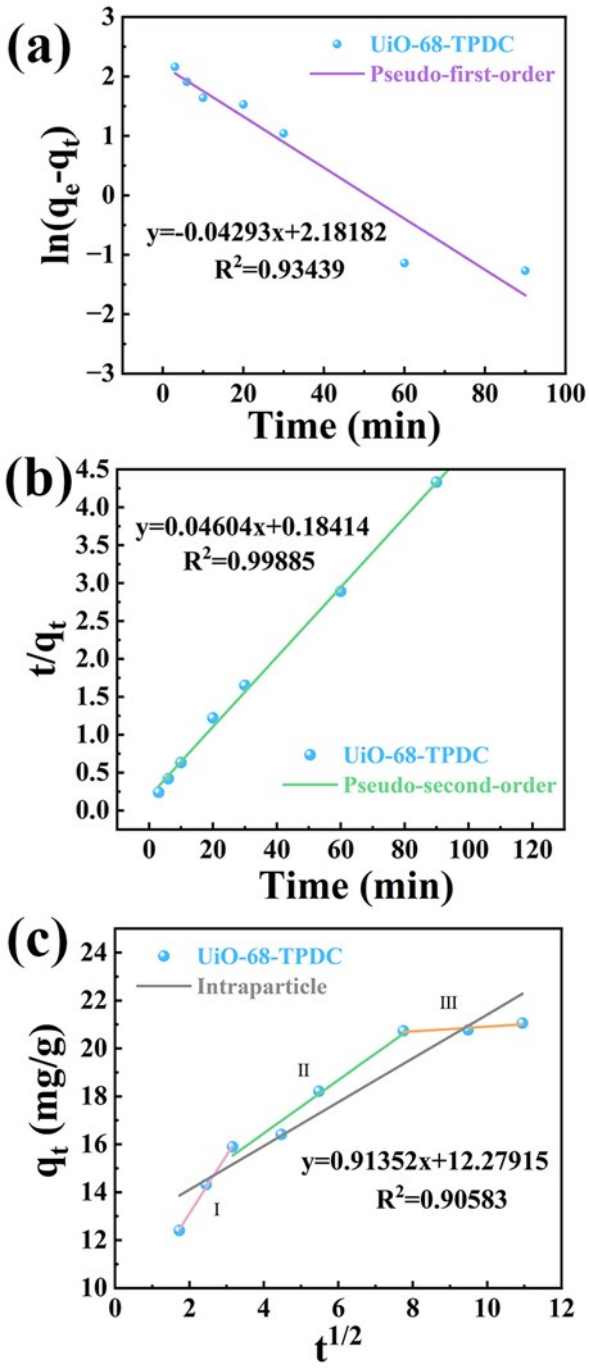

Fig. S8. Kinetic fitting plots for Au(III) adsorption on UiO-68-TPDC.

(a) Linear plot of the pseudo-first-order kinetic model. (b) Linear plot of the pseudo-second-order kinetic model. (c) Intraparticle diffusion model plot, showing the multi-stage diffusion behavior of Au(III) on UiO-68-TPDC

Table S1. Intraparticle diffusion model parameters for Au(III) adsorption on UiO-68-TZDC and UiO-68-TPDC.

Adsorbent	Parameters	Part I	Part II	Part III
UiO-68-TZDC	C	14.81801	19.07755	25.21419
	k_3	2.54577	1.26365	0.46993
	R^2	0.99905	0.98878	0.83486
UiO-68-TPDC	C	8.2308	12.02963	19.93323
	k_3	2.44109	1.10841	0.09756
	R^2	0.99711	0.96643	0.80362

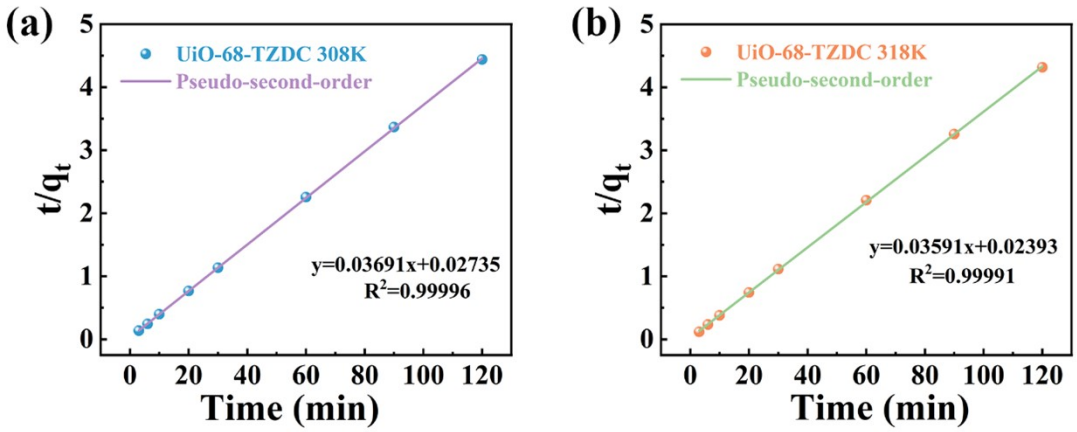

Fig. S9. Pseudo-second-order (PSO) kinetic model fitting for Au(III) adsorption on UiO-68-TZDC at (a) 308 K and (b) 318 K.

Table S2. Pseudo-second-order kinetic parameters at 308 and 318 K.

Adsorbent	T (K)	k_2 (g/mg/min)	q_e (mg/g)	R^2
UiO-68-TZDC	308	0.04981	27.093	0.99996
	318	0.05389	27.847	0.99991

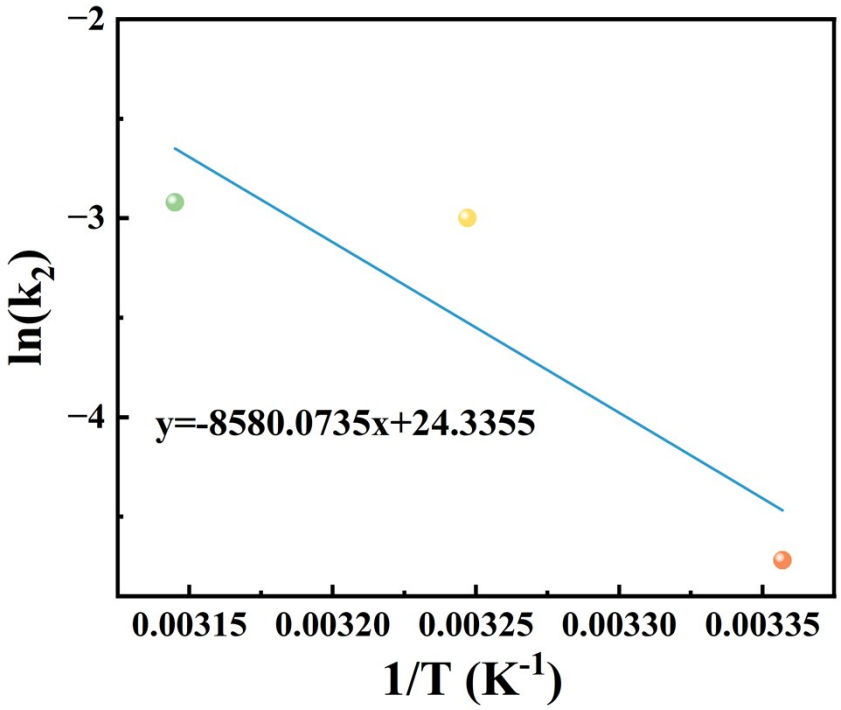

Fig. S10. Arrhenius plot of $\ln(k_2)$ versus 1/T for Au(III) adsorption on UiO-68-TZDC, where k_2 is the pseudo-second-order rate constant obtained at different temperatures (25-45 °C). The apparent activation energy (E_a) was determined from the slope of the linear fit.

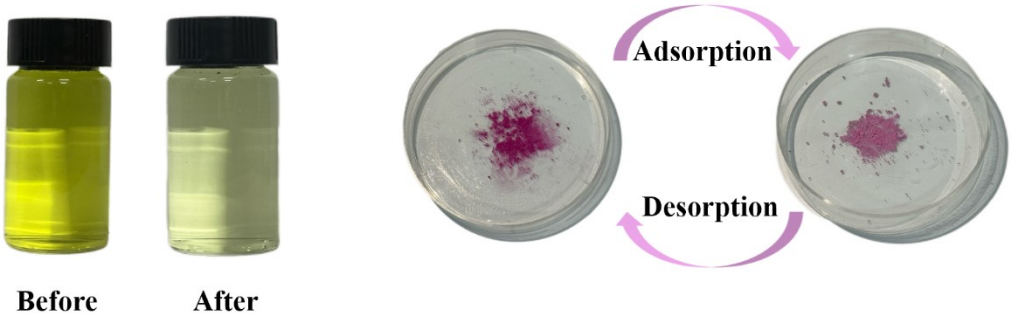

Fig. S11. Photographs of Au(III) solution and UiO-68-TZDC before and after adsorption. The yellow Au(III) solution becomes nearly colorless after contact with UiO-68-TZDC (left), indicating efficient removal of Au(III). The UiO-68-TZDC powder gradually turns deep purple after adsorption and is partially restored after desorption (right), demonstrating the enrichment of Au species on the adsorbent and its regenerability under the standard conditions described in the text.

Table S3. Comparison of saturated adsorption capacities for Au(III) on different adsorbents

Adsorbent	pH Value	Adsorption Capacity (mg/g)	Ref.
UiO-68-TZDC	3.0	404.4	This work
UiO-68-TPDC	3.0	114.5	This work
MOF-AFH	5.0	389.0	5
UiO-66-NH_2	3.0	166.2	6
UiO-66-MTD	6.0	301.5	7
UiO-66-ATU	3.0	227.7	8
UiO-66-TA	2.0	372.0	9
ZT-MOF	7.0	333.3	10
TTB-COF	—	560.0	11
UiO-66-BTU	2.0	680.2	6

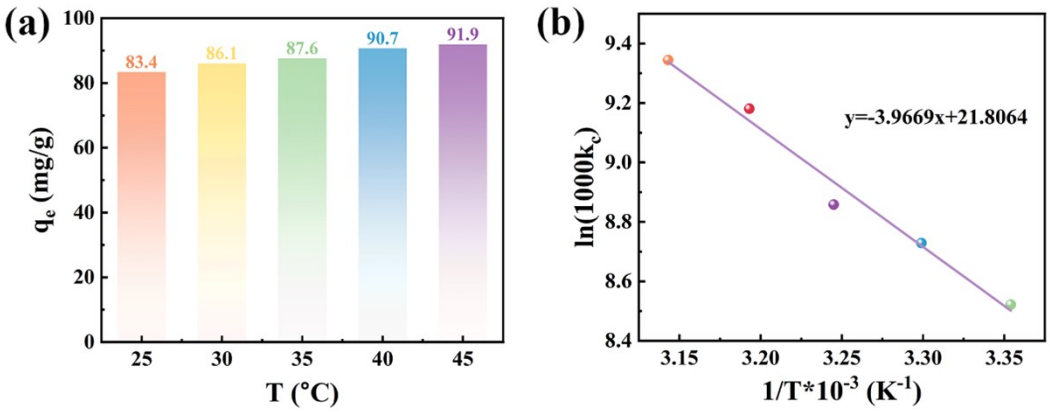

Fig. S12. (a) Effect of temperature on the equilibrium adsorption capacity (q_e) of Au(III) on UiO-68-TZDC (25-45 °C, corresponding to 298-318 K). (b) van't Hoff plot for Au(III) adsorption on UiO-68-TZDC.

Table S4. Thermodynamic parameters for Au(III) adsorption on UiO-68-TZDC at different temperatures.

Adsorbent	T (K)	△G (kJ/mol)	△H (kJ/mol)	△S (J/mol·K)
UiO-68-TZDC	298	-21.07	32.98	181.30
	303	-21.98		
	308	-22.89		
	313	-23.79		
	318	-24.70		

.

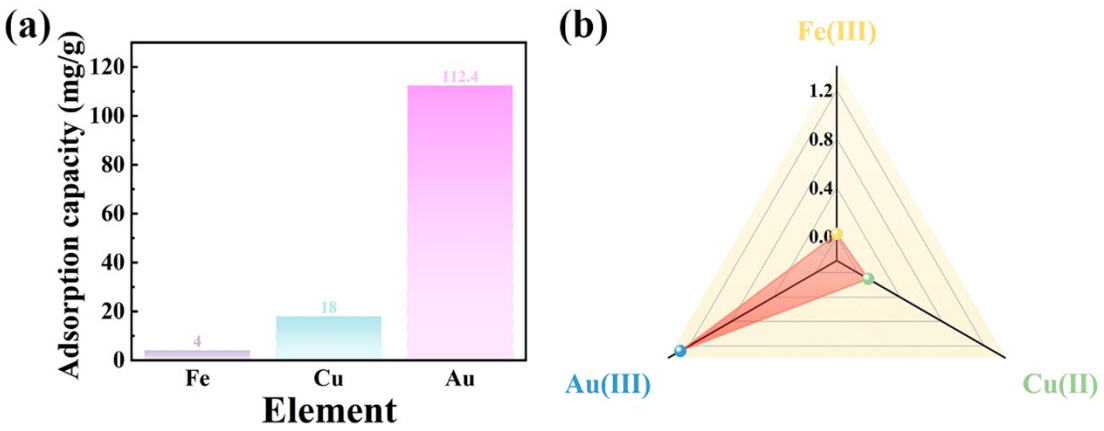

Fig. S13. (a) Adsorption capacities of UiO-68-TZDC toward Fe(III), Cu(II) and Au(III) in a mixed-metal solution. (b) Distribution coefficients (D) for the competitive adsorption of Fe(III), Cu(II) and Au(III) on UiO-68-TZDC, illustrating the preferential uptake of Au(III).

Table S5. Distribution coefficient (D) and selectivity coefficient (k) of UiO-68-TZDC toward different metal ions (Fe, Cu, and Au).

Metal ions	Distribution coefficient (D) (L/g)	Selectivity coefficient (k)
Fe	0.02041	62.87
Cu	0.09890	12.97
Au	1.28311	1

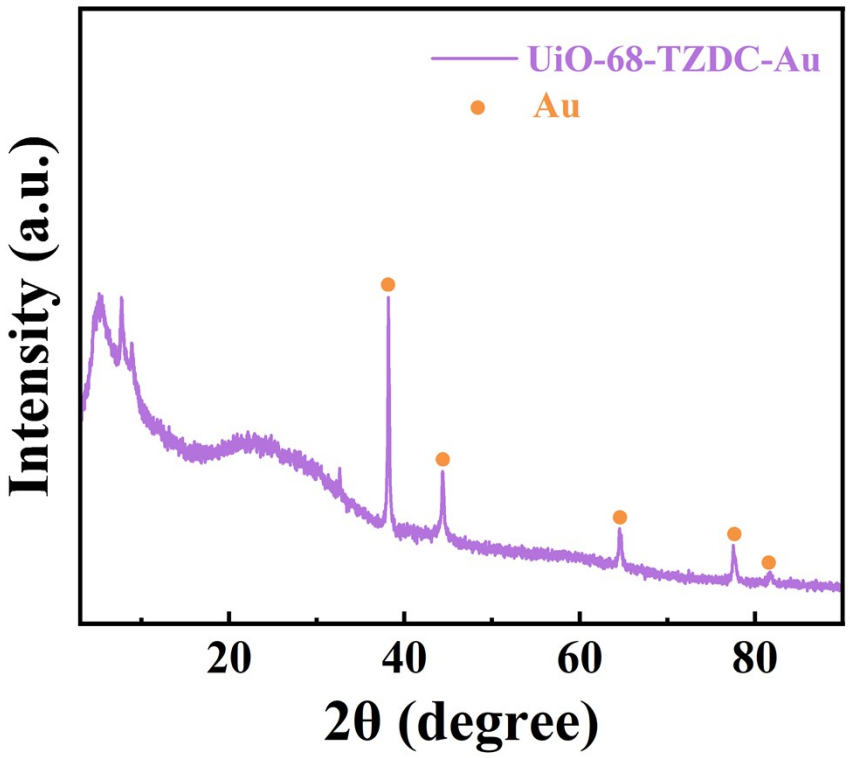

Fig. S14. PXRD patterns of UiO-68-TZDC after Au(III) adsorption. The marked diffraction peaks correspond to the characteristic reflections of metallic Au, indicating that part of Au(III) is reduced to Au(0) and deposited in the material during the adsorption process.

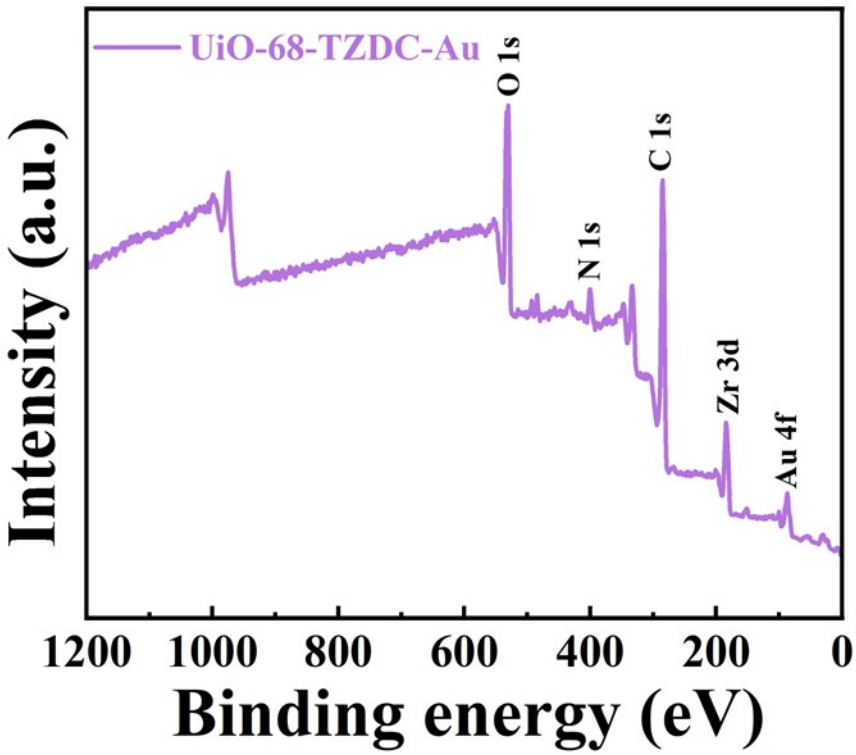

Fig. S15. XPS survey spectrum of UiO-68-TZDC after Au(III) adsorption, showing characteristic peaks of C 1s, N 1s, O 1s, Zr 3d and Au 4f.

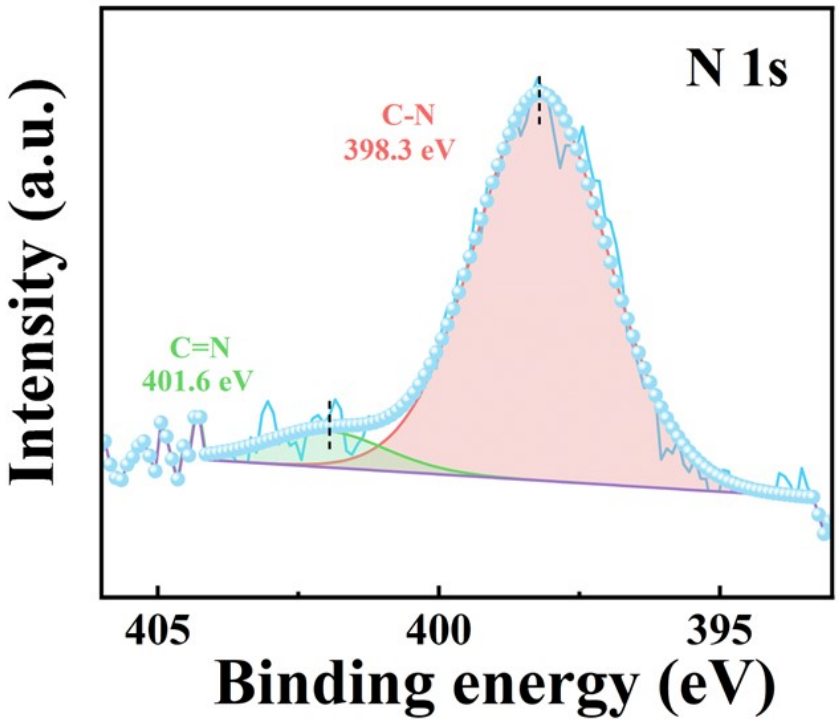

Fig. S16. N 1s XPS spectra of UiO-68-TZDC after Au(III) adsorption.

As shown in Fig. S16, the C–N and C=N components in the N 1s spectrum of UiO-68-TZDC shift to higher binding energies after Au(III) adsorption.

References

1 J. Wang and X. Guo, J. Hazard. Mater., 2020, 390, 122156.

2 H. He, X. Yang, S. Li, Y. Xu, S. Ye, M. Xiong, N. Yang, C. Feng, Y. Zhang and Z. Nie, Sep. Purif. Technol., 2025, 376, 133945.

3 H. He, S. Li, X. Yang, Y. Xu, W. Du, S. Ye, H. Dong, X. Zhao, N. Yang, Y. Zhang and Z. Nie, Sep. Purif. Technol., 2025, 378, 134543.

4 Y. Zhang, H. Dong, W. Du, C. Dong, M. Xiong, N. Yang, S. Zhao, H. He and Z. Nie, Chem. Eng. J., 2025, 505, 159419.

5 J. Tang, Y. Chen, S. Wang, D. Kong and L. Zhang, Environ. Res., 2022, 210, 112870.

6 J. Guo, X. Fan, J. Wang, S. Yu, M. Laipan, X. Ren, C. Zhang, L. Zhang and Y. Li, Chem. Eng. J., 2021, 425, 130588.

7 C. Wang, G. Lin, J. Zhao, S. Wang and L. Zhang, Chem. Eng. J., 2020, 388, 124221.

8 M. Zhao, Z. Huang, S. Wang, L. Zhang and C. Wang, Microporous Mesoporous Mater., 2020, 294, 109905.

9 C. Wang, G. Lin, J. Zhao, S. Wang, L. Zhang, Y. Xi, X. Li and Y. Ying, Chem. Eng. J., 2020, 380, 122511.

10 Z. Huang, M. Zhao, S. Wang, L. Dai, L. Zhang and C. Wang, J. Mol. Liq., 2020, 298, 112090.

11 Z. Zhou, W. Zhong, K. Cui, Z. Zhuang, L. Li, L. Li, J. Bi and Y. Yu, Chem. Commun., 2018, 54, 9977–9980.